

## Over 8 hours of continuous operation of a free-electron laser driven by a laser-plasma accelerator

F. Kohrell<sup>1,2,\*</sup>, S. K. Barber<sup>1</sup>, C. E. Doss<sup>1</sup>, K. Jensen<sup>1</sup>, S. Schröder<sup>1</sup>, C. Berger<sup>1,3</sup>,  
Z. Eisentraut<sup>1</sup>, K. Nakamura<sup>1</sup>, A. J. Gonsalves<sup>1</sup>, F. Isono<sup>1,3</sup>, G. R. Plateau<sup>4</sup>,  
R. A. van Mourik<sup>4</sup>, M. Gracia-Linares<sup>4</sup>, L. Labun<sup>4</sup>, B. M. Hegelich<sup>4</sup>, S. V. Milton<sup>4</sup>,  
C. G. R. Geddes<sup>1</sup>, J. Osterhoff<sup>1</sup>, E. H. Esarey<sup>1</sup>, C. B. Schroeder<sup>1,3</sup>,  
F. Grüner<sup>2</sup> and J. van Tilborg<sup>1</sup>

<sup>1</sup>Lawrence Berkeley National Laboratory, Berkeley, California 94720, USA

<sup>2</sup>University of Hamburg and Center for Free-Electron Laser Science,  
Luruper Chaussee 149, 22761 Hamburg, Germany

<sup>3</sup>University of California, Berkeley, California 94720, USA

<sup>4</sup>Tau Systems Inc., Austin, Texas 78701, USA



(Received 17 July 2025; accepted 13 February 2026; published 7 April 2026)

Since the emergence of laser-plasma accelerators (LPAs), substantial work has been dedicated to using LPAs to drive free-electron lasers (FELs) for a broad range of applications. Despite recent breakthroughs, which have proven the fundamental feasibility of operating FELs with an LPA source, stable FEL operation over multiple hours without operator input had yet to be achieved. In this work, we report significant improvements to the stability of a hundred terawatt laser system, resulting in successful demonstration of reliable, long-term operation of an LPA-driven FEL in the self-amplified spontaneous emission (SASE) regime at 420 nm. The LPA source delivered 100 MeV electron beams at 1 Hz with high stability over more than 10 h, enabling over 8 h of continuous FEL operation without operator input. The acquired data were subsequently used to investigate correlations between the measured undulator radiation and parameters of the drive laser, plasma source, and electron beam. The revealed connections between LPA and FEL performance gave important additional insights into ways to further improve and stabilize the system, thus demonstrating the capability of our setup to serve as a powerful platform for future studies of LPA-driven FEL operation. The one-of-a-kind integration of multiple stabilization concepts onto the LPA facility discussed in this manuscript yielded significant accelerator and light source improvements (with residual correlations suggesting even more is possible), which will positively impact LPA applications at large.

DOI: [10.1103/z2d3-bhyt](https://doi.org/10.1103/z2d3-bhyt)

### I. INTRODUCTION

Laser-plasma accelerators (LPAs) [1,2] provide a compact source of electron beams with energies up to 10 GeV [3–6]. The charged particles are accelerated in plasma wakefields excited by laser drivers, exploiting the high field strengths of 10–100 GV m<sup>-1</sup>, far exceeding the values achievable in radio-frequency (rf)-based accelerators [2]. Due to the demonstrations of high beam quality achievable in LPAs [7–12] and their intrinsic advantages of small footprint and potential to generate ultrashort and high brightness electron beams, they quickly became a promising source for novel light sources, including compact

x-ray free-electron lasers (FELs) [13–19]. Despite their many promising characteristics, LPAs face inherent challenges in shot-to-shot stability, especially in the context of the strict tolerance requirements of FELs. The properties of the plasma wake are intrinsically connected to the driving laser pulse, making the generated electron beams highly sensitive to instabilities of the drive laser. Fluctuations of transverse focal position [20], longitudinal focal position [21], pulse energy [22], and pulse duration [23] of the laser, among others, have been demonstrated to impact LPA performance. Because reliable FEL operation requires exceptional electron beam stability, not only in energy, bunch length, and charge, but also in transverse beam position, a high degree of stability of the laser-plasma interaction is necessary [24,25]. First experimental results of electron beams from laser-plasma accelerators used to drive FELs demonstrated the general viability of the technology [15–17], and an experiment conducted and recently published by Barber *et al.* [17] pushed the boundaries of shot-to-shot stability and the level of

\*Contact author: [finnkohrell@lbl.gov](mailto:finnkohrell@lbl.gov)

Published by the American Physical Society under the terms of the *Creative Commons Attribution 4.0 International* license. Further distribution of this work must maintain attribution to the author(s) and the published article's title, journal citation, and DOI.

observed gain, but further improvements, especially in performance and reliability [18], are required for them to emerge as practical options for future light source facilities. Aside from their application specifically for FEL light sources, LPAs have been proposed to power the next generation of particle accelerators and colliders, as well as a host of other near-term applications in the medical, security, and microelectronics domain. Impacted by the above-mentioned fundamental sources of instability, improving the reliability of LPAs and the quality of their generated electron beams has been identified by the community as key steps toward realizing the technology’s full potential [26,27].

In a recent publication by Barber *et al.* [17], the authors of the work presented here demonstrated a breakthrough in shot-to-shot reliability and peak performance of LPA-driven FELs on the 1 h timescale. In this work, we report significant advances toward achieving the same level of reliable, high-gain performance of LPA-driven FELs over many hours of continuous operation, without the need for active operator intervention. To enable the high level of long-term stability demonstrated here, a variety of different methods were employed to stabilize the LPA interaction, including active stabilization of the transverse and longitudinal position of the laser beam, as well as the laser pulse duration and energy. The results discussed here serve as evidence that the strict requirements for stability of the electron beam, plasma source, and laser pulse stability can be realized reliably over many hours of continuous operation. Furthermore, the large amount of gathered diagnostic data enables excellent opportunities to study and identify correlations between LPA parameters and FEL performance. From these studies, informative models of the LPA-FEL process can be developed to assist in improved overall characterization of the system. This work thereby represents a critical step, not only toward the development of LPA-driven FELs as a competitive light source technology, but also for LPAs in general to reach their full potential as powerful, next-generation accelerators.

## II. EXPERIMENTAL SETUP

This section will give an overview of the experimental setup of the LPA-FEL system used for the experiments described in this work. The following tables identify key parameters for the experiment that are actively stabilized (see Table I) or monitored only (Table II), and the related acronyms.

### A. Laser system and electron beamline

As shown schematically in Fig. 1, the laser used for electron generation and acceleration on the BELLA Center’s Hundred Tera-Watt Undulator (HTU) system is a titanium-sapphire (Ti:Sapph)-based chirped pulse amplification [28] system delivering pulses in the 100 TW

TABLE I. Active stabilization systems.

System	Stabilized parameter	Details
TSS <sub>1</sub>	Transverse beam position and angle after stretcher	100 Hz commercial correction system
TSS <sub>2</sub>	Transverse beam position on first amplifier (Amp1)	Custom long-term drift correction
TSS <sub>3</sub>	Transverse beam centroid $r$ on second amplifier (Amp2)	300 Hz commercial two-stage stabilization
LSS	Longitudinal position of laser focus via radius of curvature (ROC) control	32 Hz closed-loop wave front sensor (WFS) feedback
TSS <sub>4</sub>	Transverse beam position at focus $r_{\text{ghost}}$	Custom stabilization using “ghost beam”

TABLE II. Diagnostic systems (monitored-only parameters).

System	Monitored parameter	Details
Energy meter (E)	Laser pulse energy $E_p$	Noninvasive measurement
GRENOUILLE	Temporal ( $D2\sigma_{\text{temp}}$ ), spectral ( $D2\sigma_{\text{spectr}}$ ) pulse properties	Noninvasive single-shot SHG-FROG
Wave front sensor (WFS)	Plasma density profile (shock angle, density $\Delta n$ , slope)	Noninvasive synchronized ( $D$ ) probe beam
Charge monitor (ICT 1 and ICT 2)	Electron bunch charge $q$	Upstream and downstream of undulator
Magnetic spectrometer (MagSpec 1 and MagSpec 2)	Electron bunch energy $E_b$ , rms energy spread $\sigma_E$	Upstream and downstream of undulator
VISA probes	Electron beam profile, undulator signal energy $U(q)$	YAG:Ce screens, optical spectrometer along undulator

regime to the target area. The laser front-end is based on an 80 MHz Ti:Sapph oscillator followed by a regenerative amplifier, delivering 38 fs, 800 nm, 2.5 mJ pulses at a repetition rate of 1 kHz. To avoid damaging sensitive optics during and after the next amplification stage, the pulses are subsequently stretched to a pulse duration  $\tau$  of 290 ps. A Pockels cell (PC) after the stretcher increases the ns-scale pulse contrast of the kHz pulse train. Three multipass stages make up the main amplifier chain, pumped at 532 nm by a 16 J, 16 ns frequency-doubled Nd:YAG laser operating at 1 Hz. These amplifiers increase the final pulse  $E_p$  to a maximum of 5 J. Each of the three amplifiers (Amp1–3) shown schematically in Fig. 1 represents a more complex,

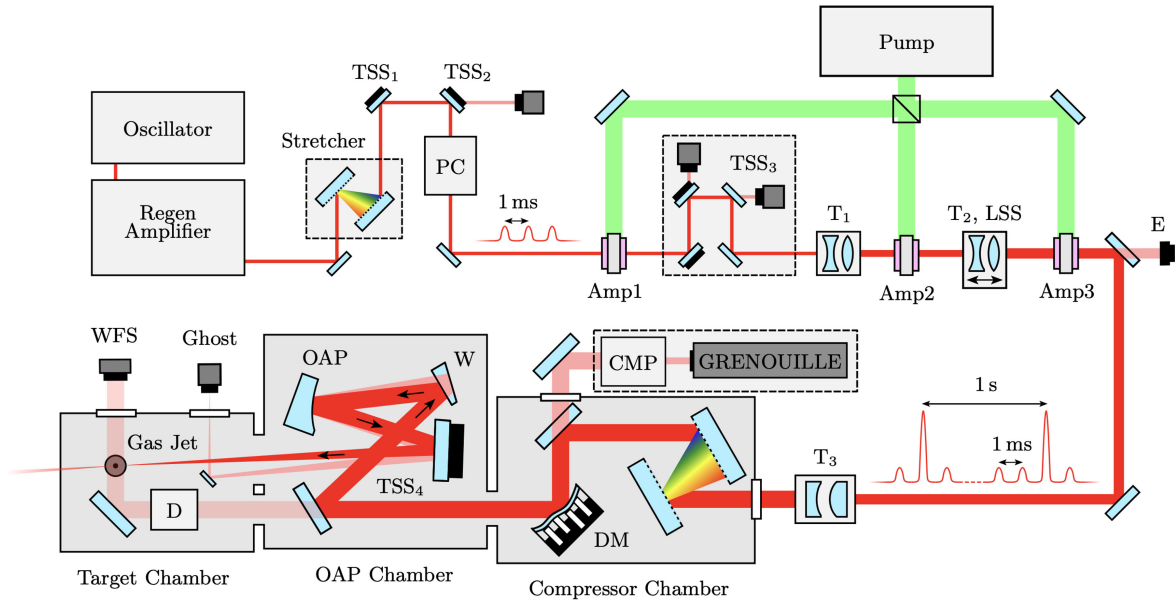


FIG. 1. Schematic display of the Hundred Terawatt Undulator (HTU) laser beamline. The beam angle and centroid position are actively corrected by a transverse stabilization system (TSS<sub>1</sub>) through the Pockels cell (PC). A custom (TSS<sub>2</sub>) and a commercial (TSS<sub>3</sub>) setup are used to stabilize transverse beam positions on the three amplifier crystals (Amp1, 2, and 3). T<sub>1</sub> and T<sub>2</sub> are transmissive and T<sub>3</sub> is a reflective beam expander telescope. The second lens in T<sub>2</sub> is mounted on a motorized stage to act as a longitudinal stabilization system (LSS). After amplification, the beam energy is noninvasively monitored (E). A leakage beam sent to the chirped mirror compressor (CMP) and GRENOUILLE allows monitoring of spectral and temporal pulse properties. The deformable mirror (DM) optimizes pulse wave front quality. After the DM, a synchronized, leaked copy of the laser beam is timed through a delay line (D) and used as a probe for the plasma density profile through detection by a wave front sensor (WFS). A wedged mirror (W) creates a low-intensity copy of the main beam (ghost beam), with both the high-intensity front-surface reflection and this low-power ghost beam replica focused by the off-axis parabolic mirror (OAP). The final steering mirror (TSS<sub>4</sub>) is used for active stabilization of the main beam transverse position on target.

four-pass amplification setup, which was simplified for display purposes. To reduce beam intensity on the optics during and after the amplification process, the beam diameter is expanded multiple times from 6 to 23 mm via three telescope stages interleaved with the amplification stages. After the final amplification stage, the beam is expanded by a reflective mirror telescope T<sub>3</sub> to a diameter of 81 mm FWHM, and subsequently transmitted into the vacuum system. The grating-based compressor returns the pulse duration  $\tau$  from 290 ps back to its bandwidth-limited value of 38 fs. Afterward, the beam is sent onto a deformable mirror (DM) which optimizes the pulse wave front. A 3 m focal length OAP focuses the beam and delivers an amplified 38 fs pulse of energy  $E_p$  up to 2.5 J at 1 Hz to a spot of 40  $\mu\text{m}$  FWHM onto the gas jet target.

The LPA target assembly, as schematically displayed in Fig. 2(a), consists of a rigidly mounted blade above the supersonic gas jet. This creates a density shock  $\Delta n$  in the gas profile and enables generation of electron beams through the down-ramp injection process [25,29–31]. To control and tune the injection, the position of the gas jet assembly and the relative position of the blade are adjustable. Helium gas at 200 psi (1.38 MPa) is supplied to the gas jet, and the assembly is tuned to produce electron

beams of 100 MeV central energy  $E_b$ , as can be seen in Fig. 2(b). These beams exhibit a central energy rms jitter on the order of 5 MeV, with 3%–6% rms energy spread  $\sigma_E$  and average bunch charge  $q$  of 80 pC and rms jitter of 30 pC. Beams of finite energy spread and divergence are subject to intrinsic chromatic emittance growth [32]. To reduce this effect and control the electron beam divergence after the plasma target, a permanent magnet quadrupole (PMQ) triplet is placed as close as 3.5 cm behind the interaction point. For precise alignment to the beam axis, the PMQ triplet is mounted on a hexapod that provides full translation and rotation control (6 degrees of freedom).

A magnetic chicane [33] 1 m behind the plasma source serves multiple purposes for the experiment. Most importantly, it reduces the electron bunch slice energy spread by stretching the bunch, which can reduce the FEL gain length [34]. By adjusting the field strength of the dipole pairs, which controls the momentum compaction factor of the chicane ( $R_{56}$ ), the transmitted electron bunch can be stretched by a controlled amount. For the experiments discussed in this work, the chicane was set to generate an  $R_{56}$  of 150  $\mu\text{m}$ . This value was found experimentally to deliver the best FEL performance. Additionally, the magnetic chicane separates the electron beam path from the

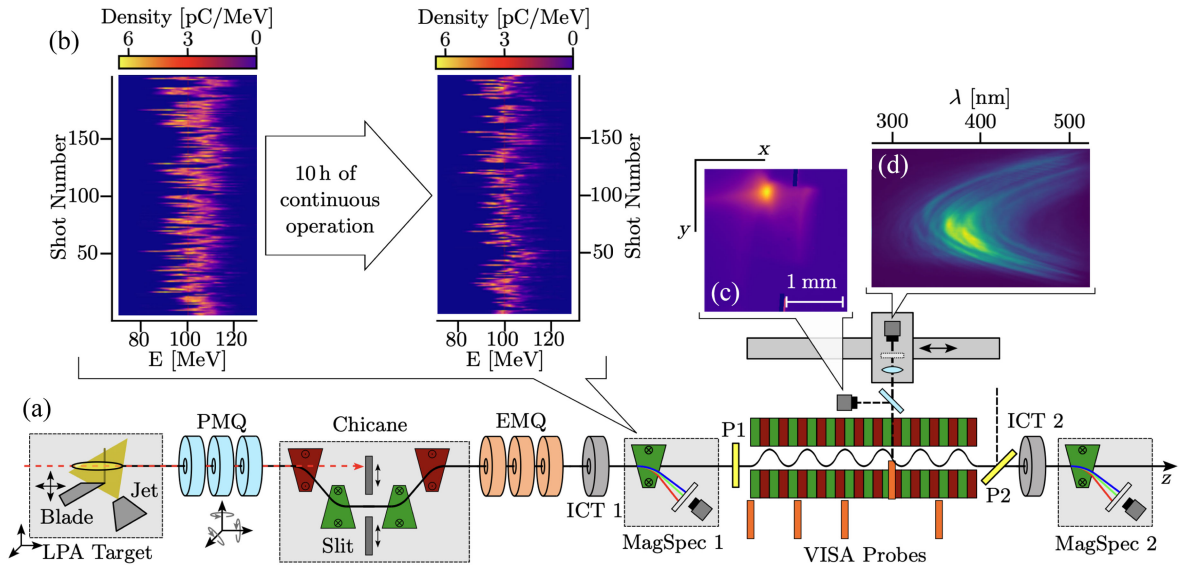


FIG. 2. (a) A schematic of the target assembly used on the HTU system and the subsequent electron beamline to the VISA undulator, including diagnostics. The laser pulse (red dashed line) is focused onto the density down-ramp plasma target, and the generated electron beam (black solid line) is focused (PMQ), longitudinally stretched (magnetic chicane), and refocused (EMQ) before being sent into the VISA undulator. Integrating current transformers (ICT 1 and ICT 2) and magnetic spectrometers (MagSpec 1 and MagSpec 2) measure electron beam charge and energy before and after the undulator. A thin pellicle (P1) upstream of the VISA can be used to spoil the beam emittance, and a reflective pellicle (P2) downstream to measure undulator signal while transmitting the electron beam. (b) 100 consecutive electron beam spectra recorded with the magnetic spectrometer upstream of the undulator (MagSpec 1, which can be turned on/off remotely). The two scans were taken 10 h apart, during which period no changes were made to the laser or plasma target. (c) Example of a transverse electron beam profile recorded by inserting one of eight probes spaced evenly along the length of the undulator. A dichroic mirror separates the emission from the YAG:Ce screen from the undulator radiation and sends it to an imaging camera. (d) Representative example spectrum of a high gain shot recorded in this dataset. The FEL radiation is transmitted through the dichroic mirror onto an energy calibrated optical spectrometer. The optical spectrometer is mounted on a 4 m translation stage that allows placement at any of the probe locations.

laser axis, as can be seen schematically in Fig. 2(a). By inserting an adjustable tungsten slit, the laser is blocked and only the electrons at a defined transverse offset from the main axis and with a certain energy are transmitted, limiting unwanted background signal and preventing damage to more sensitive electron beam diagnostic equipment. After the chicane, the electron beam passes through an electromagnetic quadrupole (EMQ) triplet, which matches it to the undulator.

The undulator used in the HTU beamline, originally named visible to infrared SASE amplifier (VISA) undulator [35], was designed and built to be used at Brookhaven National Lab for one of the first experimental demonstrations of full saturation in the SASE regime [36,37]. It consists of four 1 m long sections that are embedded in a vacuum chamber. There is no free drift space between the segments, and each section contains 55 periods (220 total). With a root-mean-square (rms) undulator parameter  $K = 0.9$  and undulator period  $\lambda_u = 1.8$  cm, the resonant wavelength when using electrons at 100 MeV is 420 nm. Because the magnetic structure of the VISA undulator has integrated external periodic focusing, matching the electron beam Twiss parameters to its FODO lattice via the EMQ triplet is crucial [38,39].

## B. System stabilization and diagnostic capabilities

This section introduces the currently employed “transverse stabilization systems” (TSS) to actively control the laser position centroid  $r$  at multiple positions throughout the laser system (TSS<sub>1</sub>-TSS<sub>4</sub>), as well as the “longitudinal stabilization system” (LSS) to control the laser pulse radius of curvature (ROC). Additional parameters, like the laser pulse energy  $E_p$ , duration  $\tau$ , plasma density  $n$ , as well as energy  $E_b$  and charge  $q$  of the electron beam, are monitored passively for correlation studies.

The HTU laser system includes multiple stages of stabilization for the transverse beam position before the final focus and LPA target location. As can be seen in Fig. 1, the transverse position of the beam and incident angle on the Pockels cell (PC) are actively stabilized after the stretcher using a commercial two-stage system (represented schematically by a single mirror in Fig. 2 as TSS<sub>1</sub>) offering  $\sim 100$  Hz correction bandwidth through fast acting piezo actuators. The position of the beam on the first amplifier crystal is stabilized against long-term drift using a custom, single-stage beam pointing stabilization (TSS<sub>2</sub>).

During and after amplification of the laser pulse in the main amplifier, the unamplified 1 kHz, mJ-level pulse train co-propagates with the 1 Hz amplified pulses,

as schematically shown in Fig. 1. This unamplified background signal is employed for multiple diagnostic and stabilization systems because it enables a much higher correction bandwidth than using the amplified pulses at 1 Hz. To prevent saturation or damage to diagnostics detecting the 1 kHz unamplified pulses caused by the much stronger amplified 1 Hz signal, different techniques, such as mechanical shutters or a separate trigger signal, which stops acquisition for a few milliseconds around the amplified pulses, are employed. The transverse beam position centroid  $r$  between the first (Amp1) and second multipass amplifier crystal (Amp2) is controlled by a commercial, two-stage active stabilization system (TSS<sub>3</sub> in Fig. 1), which includes position sensitive device detectors with  $<0.5 \mu\text{m}$  spatial resolution. The mirrors for active stabilization are piezo-driven and support  $>300$  Hz correction bandwidth by using the unamplified 1 kHz pulse train for active feedback.

The laser pulse energy  $E_p$  is monitored noninvasively by a calibrated, commercial energy meter (E) following the final stage of amplification. After passing through the compressor, leakage of the beam through a high-reflective optic in the compressor chamber is picked up for noninvasive, single-shot characterization of temporal and spectral pulse dynamics, based on a GRENOUILLE diagnostic. It acquires images through the nonlinear second-harmonic generation (SHG) frequency-resolved optical gating (FROG) technique, allowing full characterization of the laser pulse spectral amplitude and phase with a single shot [40,41]. The design and characterization of this diagnostic setup has been described in detail by Kohrell *et al.* in Ref. [23].

Before the final focusing optic, a 99% beam splitter in the OAP chamber creates a 1%-leakage probe beam which traverses the plasma target orthogonally to the main laser. A delay stage (D in Fig. 1) synchronizes the probe and main laser pulse, and a high resolution wave front sensor (WFS) monitors the phase imprint on the probe beam from the plasma target, which can be used to estimate the plasma profile [42].

For monitoring and stabilization of the beam position in the focal plane of the OAP, a low-intensity copy of the main beam is created using a wedged optic (W, see Fig. 1). Its front surface has a 99% reflective coating, and its back surface one of  $>99.5\%$ . The angle of the wedge was designed such that the front (main beam) and back surface (ghost beam) reflection overlap on the OAP, with an angular separation of  $1.21^\circ$ . To monitor the beam position at focus nondestructively, the ghost beam is picked off by a mirror after the final steering optic and directed onto the detection setup outside of the vacuum system. The 1 kHz unamplified component of this ghost beam is used for stabilization of the transverse and longitudinal beam position at focus (TSS<sub>4</sub> and LSS in Fig. 1, respectively). The transverse centroid of the ghost beam  $r_{\text{ghost}}$  is

monitored with a camera and actively stabilized to a chosen setpoint via the motorized optic used for TSS<sub>4</sub>, its ROC is monitored with a WFS on the ghost line and used for closed-loop operation of the adjustable telescope T<sub>2</sub> (see Sec. III A for a more detailed description) [20,21,43].

Diagnostics for the electron beam after the LPA target include a pair of integrating current transformers (ICT 1 and ICT 2) that measure charge  $q$ , and two magnetic spectrometers (MagSpec 1 and MagSpec 2) which enable measurement and comparison of the electron bunch energy  $E_b$  before and after the undulator. A  $10 \mu\text{m}$  thick nitrocellulose pellicle (P1) was installed on a pneumatic actuator before the undulator entrance, close to where the electron beam comes to a focus. As discussed and experimentally verified by Barber *et al.* [17], it serves as an emittance spoiler by scattering the transmitted electron beam, without having significant impact on its energy or trajectory. Thus, it can serve as a way to quickly distinguish between incoherent undulator light and coherent FEL radiation.

Along the length of the undulator, eight evenly spaced ports allow characterization of the e-beam transverse profile and position with respect to the a straight line reference, as well as the generated FEL radiation spectrum and energy. This is enabled by the design of insertion probes mounted to pneumatic actuators at each port. They consist of a  $0.2 \text{ mm}$  thick,  $3 \times 3 \text{ mm}$  YAG:Ce screen and a right angle prism mirror mounted behind it, to image the electron beam profile and collect undulator radiation at the same time. Each one of the eight ports has a diagnostic setup outside the vacuum chamber with a dichroic mirror [see Fig. 2(a)], which directs the  $550 \text{ nm}$  YAG:Ce emission (e-beam profile) to a camera imaging the screen's surface [Fig. 2(c)], and the  $420 \text{ nm}$  undulator radiation to an optical spectrometer [Fig. 2(d)]. The spectrometer is custom built, energy calibrated, and has a range of  $300\text{--}550 \text{ nm}$ . A  $2''$  diameter lens  $35 \text{ cm}$  from the undulator axis focuses the undulator signal through a transmission grating onto the chip of a CCD camera. The entire undulator radiation detection setup is mounted on a  $4 \text{ m}$  long linear translation stage, which allows moving the spectrometer assembly to any port along the length of the undulator and to an additional, ninth location at the undulator exit. The final port uses a reflective pellicle (P2), reflecting the FEL radiation and transmitting the electron beam to the final magnetic spectrometer.

### III. STABILIZATION OF KEY LPA PARAMETERS

As described in Sec. I, in addition to their promising characteristics, LPAs come with their own set of unique challenges, namely the reliable and reproducible generation of high quality electron beams. Because of tight alignment tolerances due to micron-scale high-gradient cavities and the inherent property of the LPA process that a new plasma structure, which acts as the accelerating cavity, is formed on every shot, the stability of the LPA interaction strongly

affects the electron beam parameters. This also includes plasma density ( $n$ ) variations of the target. In contrast to rf accelerators, this can lead to significant shot-to-shot fluctuations. Drive laser properties (which we mainly focused on in this work), including pulse energy  $E_p$ , duration  $\tau$ , and longitudinal and transverse beam pointing, contribute most strongly [20,22].

This section gives an overview of the work done on the HTU system to mitigate these fluctuations. Work focused on the laser focal position, both longitudinal and transverse, is described in Sec. III A. Improvements to the stability of the laser pulse  $E_p$  and duration  $\tau$  are discussed in Sec. III B.

### A. Longitudinal and transverse focus position

Observations on the HTU system confirmed previously reported impact of the longitudinal focal position  $z_{\text{focus}}$  jitter and drift, quantified through measurement of the ghost beam ROC, on the stability of the e-beam source [44,45]. To address this issue, the longitudinal stabilization system (LSS) was designed and implemented. The second lens in the transmissive telescope  $T_2$  (see Fig. 1) was mounted on a motorized translation stage with cm-scale range of motion to enable control over the laser pulse radius of curvature (ROC). A WFS, sampling at 32 Hz, was installed on the ghost beamline. Closed loop operation of the two enables stabilization of the pulse's ROC to a defined value at a correction bandwidth of 0.59 Hz, completely eliminating long-term drift of  $z_{\text{focus}}$  and reducing its rms jitter by 40%. This significantly improved the stability of electron beam energy  $E_b$  and energy spread  $\sigma_E$ , making the LSS system a crucial part of enabling stable, long-term LPA operation and LPA-driven FEL studies in our system. Its design, setup, and characterization are discussed extensively by Jensen *et al.* in Ref. [21].

Similar to the change of the laser pulse ROC (and in turn the longitudinal position of the laser focus  $z_{\text{focus}}$ ), the shot-to-shot and long term variation in transverse position  $r_{\text{main}}$  of the laser beam has shown direct impact on the electron beam. This effect significantly limited the stability of the electron beams delivered to the undulator and prohibited reliable FEL operation. Using the unamplified, 1 kHz component of the ghost beam described in Sec. II, the transverse beam position  $r_{\text{main}}$  can be actively stabilized (TSS<sub>4</sub> in Fig. 1). The design of the passive monitoring and active stabilization system has been extensively studied and discussed by Isono *et al.* [43] and Berger *et al.* [20]. They were able to show the strong correlation between the transverse position of the ghost ( $r_{\text{ghost}}$ ) and main laser beam ( $r_{\text{main}}$ ), proving that the ghost beam can be used as an effective, higher frequency proxy for the high-power laser on target. Furthermore, the active stabilization of  $r_{\text{main}}$  on target, utilizing the ghost beam, was shown to drastically reduce the transverse jitter  $\Delta r_{e^-}$  of the electron beam. This makes it a powerful tool for increasing the stability

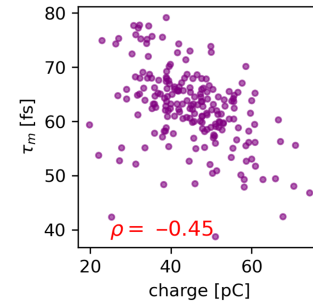


FIG. 3. Correlation between the laser pulse duration  $\tau_m$  measured with the noninvasive, single-shot GRENOUILLE diagnostic, and electron bunch charge. The strength of the correlation is quantified by the parameter  $\rho$ .

of matching the electron beam to the magnetic structure of the undulator.

### B. Laser pulse energy and duration

In addition to the position of the laser focus  $r_{\text{main}}$ , key parameters of the laser pulse, especially its energy  $E_p$  and duration  $\tau$ , affect the laser-plasma interaction [22].

The laser pulse duration  $\tau$ , in particular, has been previously found to affect LPA performance on the HTU system, as can be seen by the strong inverse correlation in Fig. 3, which matches theoretical expectations. Note that the measured pulse duration  $\tau_m$  differs from the pulse duration on target  $\tau$  (which is compressed to its bandwidth limited duration of  $\tau_0 \sim 38$  fs), due to a constant offset in dispersion added by transmission through additional material in the diagnostic line. This way of operating the diagnostic has proven advantageous to resolve small changes in dispersion witnessed by the laser pulse and has been investigated and discussed in detail by Kohrell *et al.* in Ref. [23].

In addition to the above-discussed variations of the measured pulse duration  $\tau_m$  and their impact on LPA performance, in the past we observed noticeable change of the pulse energy  $E_p$  on the order of 5% accumulating over a whole day of operation, as well as simultaneous slow drift of the beam position on the amplifier table. The correlation between beam centroid  $r$  on final amplifier crystal and  $E_p$  can be seen in Fig. 4(c), and explained by the changes in gain when the overlap between the pump and seed laser profile varies. Note, the pump beam position and profile are far more stable than the seed beam over these timescales. Manual corrections of the transverse beam position in the amplifier were able to counteract the observed energy drift, which motivated the implementation of a more robust, active solution.

A commercial, two-stage beam stabilization system (TSS<sub>3</sub> in Fig. 1) was installed between the first and second amplifier stage. It has been shown to reduce the shot-to-shot rms jitter of the beam centroid  $r$  by a factor of 9.25. To investigate its effectiveness in reducing long-term

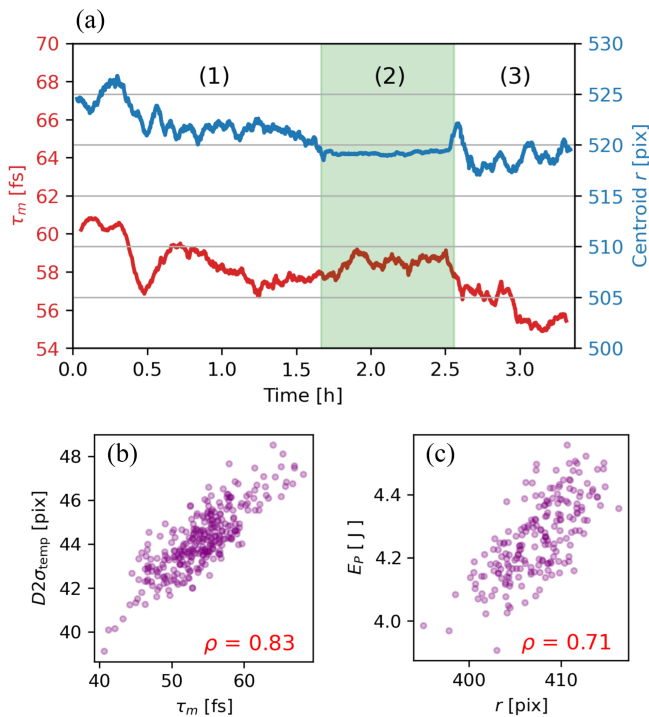


FIG. 4. Impact of the TSS<sub>3</sub> beam stabilization system on stability of key laser parameters. (a) Long-term behavior of the retrieved pulse duration ( $\tau_m$ ) and beam centroid on final amplifier crystal ( $r$ ). The stabilization system was turned OFF during the white areas of the plots (1) and (3), and turned ON during the green shaded area (2). (b) Correlation between  $D2\sigma_{\text{temp}}$  and the laser pulse duration  $\tau_m$ . (c) Correlation between the laser pulse energy  $E_p$  and  $r$ . The two correlation plots are based on a dataset from a different high-power run.

instabilities, a designated long-term measurement of over 3 h of continuous, 1 Hz laser operation was conducted. The impact of this stabilization system was tested by turning it off for the first  $\sim 90$  min (1), then activating it for roughly 1 h (2), and turning it off again for an additional  $\sim 45$  min (3), see Fig. 4(a).

The impact of this stabilization system on the laser pulse energy  $E_p$  and measured duration  $\tau_m$  was quantified through noninvasive monitoring after the main amplifier (E in Fig. 1) by recording GRENOUILLE images and using the energy meter described in Sec. II B. Using a retrieval algorithm developed by Trebino *et al.* [46,47], information about the duration  $\tau_m$  and spectrum of the measured pulse can be extracted from the acquired images. However, this technique requires a complicated and time-consuming postanalysis. By calculating the second moment  $D2\sigma_{\text{temp}}$  of the temporal axis, and  $D2\sigma_{\text{spectr}}$  of the spectral axis for each image, the dynamics of the laser pulse duration  $\tau_m$  and spectrum can be monitored qualitatively in real time and with a high degree of accuracy, as discussed in detail by Kohrell *et al.* in Ref. [23]. Therefore, this technique is employed during the experiment to monitor the spectral and temporal dynamics of the laser pulse. For the discussion in

this work, the more cumbersome postretrieval has been executed to show the trend of the measured pulse duration  $\tau_m$  over time in Fig. 4(a) directly. The strong correlation between  $D2\sigma_{\text{temp}}$  calculated from the raw images in real time and  $\tau_m$  from the postanalyzed GRENOUILLE data has been experimentally verified and can be seen in Fig. 4(b).

As can be seen in Fig. 4(a) section (1), long-term drift of  $\tau_m$  and the beam centroid  $r$  occurs over the first 1+ h of continuous operation when TSS<sub>3</sub> is off. Activating it, represented by the green shaded area (2), immediately causes a drastic improvement of the shot-to-shot stability of  $r$  (consistent with the order of magnitude improvement reported above) and eliminates long-term drift as well. The impact on the measured pulse duration  $\tau_m$  is more subtle; no obvious improvement of the shot-to-shot stability can be observed. However, the scale of long-term drift of  $\tau_m$  is reduced, underlined clearly by the drop and systematic decrease observed after the TSS<sub>3</sub> is deactivated at 2.5 h, marked by the unshaded area (3). In addition, turning the TSS<sub>3</sub> off again causes the return of strong shot-to-shot and long-term instabilities of  $r$ . This indicates a connection between the change in  $r$  and the observed drift of  $\tau_m$ . A possible explanation is that with a slow change of the beam centroid  $r$ , the laser pulse witnesses a different thickness and varying pump intensity on the crystals. The resulting difference in nonlinear effects would change the effective amount of dispersion, causing a drift of the pulse duration  $\tau_m$ .

By actively stabilizing the transverse beam position  $r$  in the amplifier chain and using the advanced diagnostic capabilities of the HTU laser system described in Sec. II, we achieve the following: improved (i) stability of the laser pulse energy  $E_p$  on long term and shot-to-shot timescales [confirmed by the strong correlation between  $r$  and  $E_p$  shown in Fig. 4(c)] and (ii) long-term stability of temporal properties of the laser. These parameters are crucial for the LPA process. This new stabilization system serves as a key tool to enable stable, long-term LPA-driven FEL operation.

#### IV. RESULTS OF LONG-TERM STABILITY STUDY

The following section will focus on the recent results demonstrating full-day ( $>8$  h) of LPA-driven FEL operation on the HTU system. They provide a follow-up to the work published recently by Barber *et al.* [17], specifically focusing on improvements to the long-term stability of the LPA-FEL system, while maintaining a level of performance comparable to the unprecedented shot-to-shot stability and gain demonstrated there.

After tuning the parameters of the LPA target and magnetic chicane, the produced electron beams were characterized on the magnetic spectrometer (MagSpec 1) before being sent to the VISA undulator, exhibiting 105 MeV average central energy, 5% central energy jitter, and about  $(5 \pm 1)\%$  energy spread. After 10 h, the measured electron beams were exhibiting an average

central energy of 102 MeV with 7% jitter, and  $(5 \pm 2)\%$  energy spread. This level of reliability was enabled through the extensive efforts to improve the long-term stability of key LPA parameters discussed in Sec. III and is essential to enable long term FEL studies.

Figure 2(b) shows the 100 consecutive shots taken on the MagSpec 1 before and after the measurement of FEL performance. Despite the various stabilization systems employed on the HTU beamline, we still noticed a modest drift in the total electron bunch charge  $q$  over more than 10 h of LPA operation, from about  $(80 \pm 30)$  pC to  $(50 \pm 25)$  pC. The exact origin of this effect is unknown at this point, but it could be caused by a number of factors. In particular, the e-beam transport system includes several apertures, such that even minor changes of the electron beam trajectory can result in charge loss. Furthermore, not all parameters of the LPA interaction are actively stabilized, the angle of the laser pulse incident on the gas jet, and the plasma target itself could be additional sources of slow drift in the system.

The thin reflective pellicle (P2 in Fig. 2) allowed us to record the reflected undulator radiation and transmitted electron beam spectrum at the same time. We optimized the undulator pulse energy  $U(q)$  using a subset of controls, including the EMQ triplet and the steering magnets controlling the launch trajectory into the undulator. Afterward, no more manipulations of the drive laser, plasma target, and electron beamline were conducted.

We measured the linear scaling of incoherent undulator radiation  $U_{\text{spont}}$  versus charge  $q$  by introducing a scattering foil. The scattering foil sufficiently spoils the emittance to prevent FEL gain [17]. The linear fit extracted from the measured data is displayed as a black dashed line in Fig. 5.

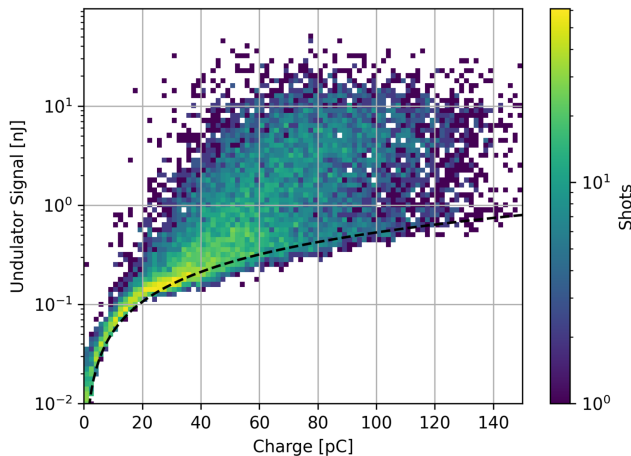


FIG. 5. Histogram of integrated undulator radiation energy  $U_{\text{total}}(q)$  (blue) for all shots taken over the  $>8$  h of continuous operation, plotted against electron bunch charge  $q$ . The black dashed curve represents the experimentally determined scaling of incoherent undulator radiation. The colorbar represents the number of shots included in each binned pixel.

It helps to visualize the shots exhibiting coherent emission, which correspond to FEL signal levels exceeding this linear scaling. To quantify the level of coherent over incoherent emission, it is useful to introduce the *coherent enhancement factor*  $F_C$ . It represents the ratio between measured FEL signal and the level of incoherent emission at a certain charge value:

$$F_C = \frac{U_{\text{total}}(q)}{U_{\text{spont}}(q)}, \quad (1)$$

where  $U_{\text{total}}(q)$  is the total measured undulator radiation pulse energy for charge  $q$  and  $U_{\text{spont}}(q)$  is the expected incoherent undulator radiation pulse energy for the same charge  $q$ . The value  $U_{\text{spont}}(q)$  is calculated based on the linear fit (counts per pC) extracted from the dataset taken using the emittance spoiler.

The measured undulator radiation energy in nJ versus charge is shown in Fig. 5.

Over half of the roughly 15,000 shots taken during this campaign exceed the level of incoherent emission, represented by the black dashed line in Fig. 5, by more than a factor of 2 ( $F_C > 2$ ).

During the experiment, a noticeable drop in average undulator radiation energy  $U_{\text{total}}(t)$  over the first 3 h of operation time  $t$  ( $\sim 6000$  shots) is observed, see Fig. 6. Afterward, there was a break in normal operations to collect ancillary data, represented in Fig. 6 by the vertical split in the plot. During this time, there were no changes to the system. Over the following 4 to 5 h of operation, the undulator signal remained largely unchanged. To quantify this change in FEL performance throughout the measurement period, we compare the average of  $F_C$  for the first and last thousand shots of the day (corresponding to a measurement period of 30 min). During the first half hour of data collection, the average coherent enhancement was  $\bar{F}_{C,1} = 9.0$ . The last half hour, after 7.5 h of continuous operation, exhibited an average coherent enhancement of  $\bar{F}_{C,2} = 4.2$ . These results demonstrate continuous and reliable LPA-driven FEL operation on the many-hour timescale. Similar to the undulator radiation signal  $U_{\text{total}}(t)$ , a reduction in the average bunch charge  $q(t)$  was observed over time, as can be seen by the blue curve in Fig. 6 and the spectra displayed in Fig. 2(b), and has been discussed above. Directly comparing the trend of  $q(t)$  to the undulator signal  $U_{\text{total}}(t)$  immediately reveals a strong correlation. The charge  $q$  exhibits a similar decrease over the first 3 h, or 6000 shots, of operation. From an average of  $\sim 80$  to  $\sim 50$  pC, this drop in LPA performance represents the most likely explanation for the observed reduction in  $U_{\text{total}}$ . The recorded instabilities of electron beam parameters should also impact the undulator radiation central energy and bandwidth. However, the low spectral resolution of the optical spectrometer during this campaign does not allow any definitive statements. In the future, efforts will be made

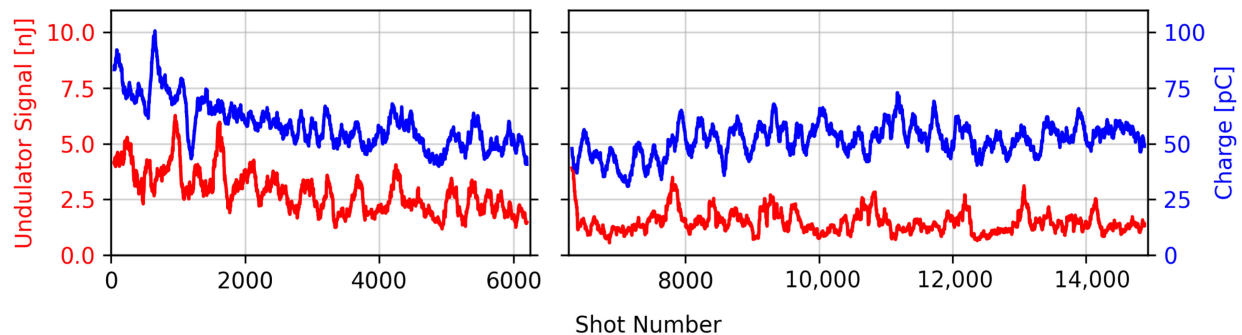


FIG. 6. Measured undulator pulse energy  $U_{\text{total}}$  (red) and electron bunch charge  $q$  (blue) over roughly 8 h of continuous operation. The gap after 6000 shots represents about an hour break, during which the electron beam trajectory through the VISA undulator was measured.

to add this capability to the diagnostic suite. Despite the 53% reduction of the measured undulator radiation energy  $U_{\text{total}}$ , after 8 h of operation, the performance and stability of both the LPA source and FEL signal nonetheless represent excellent reliability. The overall performance is still comparable to what was reported by Barber *et al.* in [17], which significantly exceeds any previously reported LPA-driven FEL performance [16,48]. And no demonstration of continuous operation for more than 1 h has ever been reported in this field. Establishing LPA-driven FELs as a viable light source technology will require reliable performance, on a level comparable to current facilities based on classical rf machines. Successfully demonstrating the HTU system as a reliable platform for full-day operation of an LPA-driven FEL therefore provides an important step toward this overarching goal. Furthermore, we have shown the capability to monitor critical laser, plasma, electron beam, and FEL radiation parameters on every shot, which gives us a unique ability to investigate potential correlations and push toward the further advancement of the field of LPA-driven light sources.

## V. INVESTIGATION OF PARAMETER CORRELATIONS

With this large dataset (>15,000 shots) including a wide variety of diagnostics (discussed in Sec. II B), we attempted to gain deeper insight into the dynamics of the system.

We calculated the Pearson correlation coefficient  $\rho$  between the measured undulator pulse energy  $U_{\text{total}}$  and over 100 recorded diagnostic parameters. Twelve of them showed a noticeable correlation and are displayed below in Table III.

The strongest correlations, exceeding an absolute value of  $|\rho| = 0.5$ , are all directly connected to electron bunch properties. They include the charge  $q$  measured upstream and downstream of the undulator with the respective ICTs (see Fig. 2), which can be seen in Fig. 5 to be naturally correlated to the undulator signal  $U_{\text{total}}(q)$ . Furthermore, the electron beam energy  $E_b$  after the undulator (measured

on every shot using MagSpec 2, see Fig. 2) shows similar correlations. Due to two noticeable peaks observed in the energy distribution, as can be seen in a spectrum recorded on MagSpec 2 averaged over 200 consecutive shots (Fig. 7), we separated the recorded spectra into two individually analyzed regions-of-interest (RoI), which allowed us to gain insight into which bunch energy distributions correlate to higher measured undulator pulse energies. However, the recorded spectra are subject to convolution with the electron beam transport up to and through the VISA undulator. Varying the steering or focusing of beam will result in changes to the observed spectrum, which are not accurate representations of actual changes of the bunch energy distribution. This convolution of  $E_b$  and beam transport, both impacting the FEL process, makes definitive statements about the origin of the two observed RoIs and their different respective correlation strengths to the undulator signal  $U_{\text{total}}(q)$  very challenging. This example was picked, however, to display the capability of utilizing the data collected during this campaign to discover previously unknown effects which are worthy of further investigations, to find pathways for future improvements of FEL stability and performance.

The laser and plasma properties showed lower correlation factors,  $|\rho| < 0.2$ . Impactful parameters include the

TABLE III. Measured parameters of the electron bunch, as well as laser pulse and plasma target, and their correlations  $\rho$  to the log of the total measured undulator radiation pulse energy  $U_{\text{total}}$ .

Electron bunch		Laser and plasma	
Parameter	$ \rho $	Parameter	$ \rho $
Charge $q$ (ICT 1)	0.69	Pulse energy ( $E_p$ )	0.09
Charge $q$ (ICT 2)	0.79	$D2\sigma_{\text{temp}}$	0.10
Energy $E_b$ (total RoI)	0.76	$D2\sigma_{\text{spectr}}$	0.15
Energy $E_b$ (low E RoI)	0.68	Shock density ( $\Delta n$ )	0.19
Energy $E_b$ (high E RoI)	0.58	Plasma shock angle	0.11
		Shock slope	0.11
		Centroid $r_{\text{ghost}}$	0.02

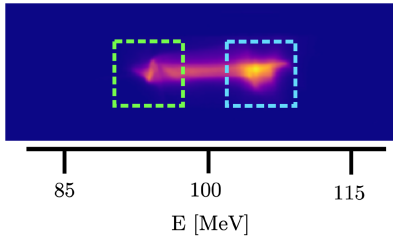


FIG. 7. Averaged electron beam spectrum of 200 consecutive shots, recorded on MagSpec 2 (downstream of the VISA undulator, see Fig. 2). The low (green) and high-energy RoI (blue) referenced in Table III have been highlighted through dashed outlines. The energy axis is based on a calibration of the phosphor screen using the dipole field strength.

laser pulse duration  $\tau_m$  and spectrum (extracted from GRENOUILLE images temporal and spectral  $D2\sigma$ ), as well as laser pulse energy  $E_p$  (measured noninvasively after the multipass amplifier, see E in Fig. 1), and the centroid  $r_{\text{ghost}}$  of the laser beam measured on the ghost line. The plasma parameters with the strongest correlations to the undulator signal are the angle of the density shock (formed by the blade above the gas jet) with respect to the laser beam, difference in density between the shock and plasma column ( $\Delta n$ ), and gradient (slope) of the density shock.

The number of parameters we were able to identify that show a noticeable correlation to the undulator radiation signal  $U_{\text{total}}$  is an indication of the high capability of the HTU system diagnostics to give valuable insights into the connections between the LPA and FEL process. To showcase some particularly interesting parameters, their correlation to the undulator radiation pulse energy  $U_{\text{total}}$  is plotted in Fig. 8.

The correlations of temporal and spectral second moments  $D2\sigma$  of the laser pulse, extracted from the raw GRENOUILLE images discussed in Sec. III B, are shown in Figs. 8(a) and 8(b), respectively. Of the two only the temporal second moment  $D2\sigma_{\text{temp}}$ , strongly correlated to the laser pulse duration  $\tau_m$  [see Fig. 4(b)], is stabilized through the active control of the laser beam centroid  $r$  in the multipass amplifier [Fig. 4(a)]. This could explain the lower correlation factor  $\rho$  for  $D2\sigma_{\text{temp}}$  of 0.1, compared to  $\rho = 0.15$  for  $D2\sigma_{\text{spectr}}$ . This result motivates further investigation of the laser pulse spectrum fluctuations, and another potential avenue to further stabilize the LPA interaction.

Figure 8(c) displays the noticeable correlation between the undulator signal  $U_{\text{total}}$  and plasma density difference ( $\Delta n$ ) between the shock feature and plasma column. There appears to be about a 20% variation of this parameter during the experiment, affecting the measured level of  $U_{\text{total}}$ . Again, this reveals a previously unknown connection between an LPA parameter and the FEL performance and will inform further studies and potential attempts at stabilization.

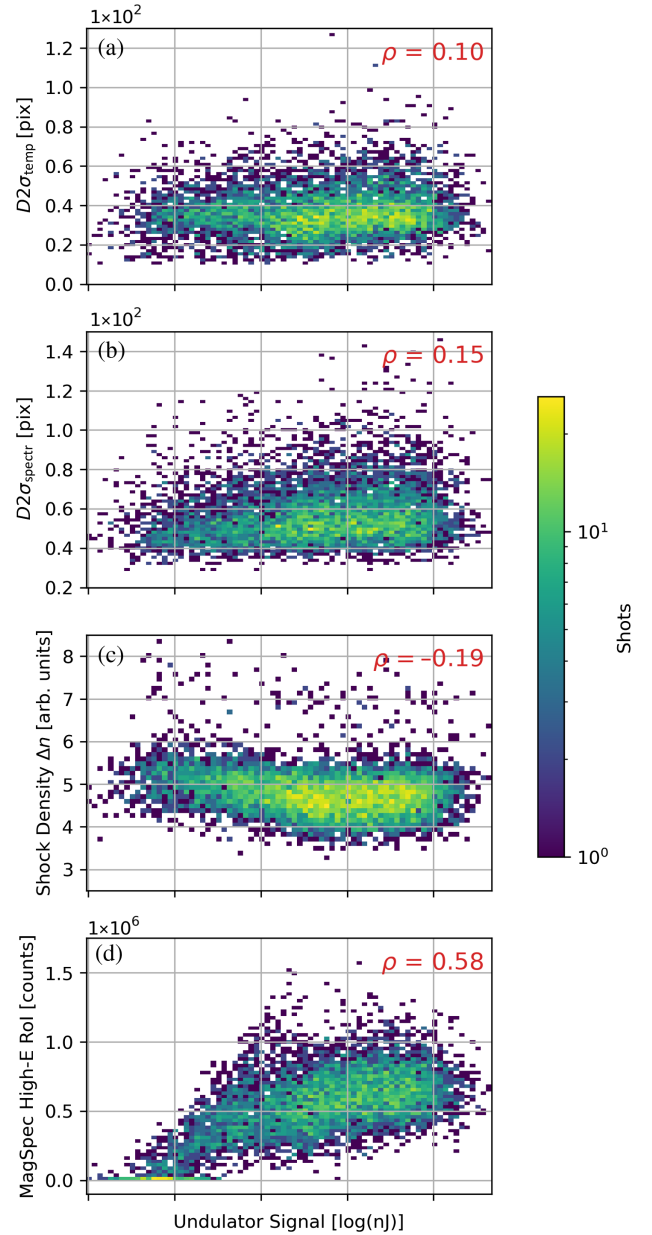


FIG. 8. Histogram of correlations between four selected LPA parameters and the undulator radiation signal, and their corresponding Pearson parameter  $\rho$ . (a) Shows the temporal, (b) the spectral second moment  $D2\sigma$  extracted from the raw GRENOUILLE images. (c) Displays the plasma density difference  $\Delta n$  between the shock and plasma column. (d) Displays the counts captured on the high-energy RoI of the magnetic spectrometer MagSpec 2 (Fig. 2).

The final parameter displayed, as can be seen in Fig. 8(d), is the counts measured on the magnetic spectrometer after the VISA undulator (MagSpec 2 in Fig. 2). Specifically, the high-energy regions-of-interest (RoI) defined based on the averaged electron beam spectra (see Fig. 7, blue dashed outline), which shows a correlation factor of  $\rho = 0.58$ . In contrast, as can be seen in Table III,

the counts measured in the low-energy RoI (see Fig. 7, green dashed outline) for the same shots display a higher correlation factor of  $\rho = 0.68$ . As discussed earlier, due to the convolution of bunch energy  $E_b$  and electron beam trajectory, explaining this observation will require further investigation.

Overall, these results are shown to demonstrate the great potential for gaining crucial new insights into how to further improve FEL performance and stability. The discovery of the apparently high impact of plasma source instabilities on LPA and in turn FEL performance is an example for further investigation and stabilization, to further increase system performance. Another goal is to develop predictive capabilities utilizing the valuable parameter correlation data discussed above, to learn if they can give us meaningful insight into crucial parameters of the FEL process, like brightness, emittance, current, and energy chirp, which are not directly monitored by our e-beam diagnostics.

## VI. SUMMARY AND OUTLOOK

In this work, we have demonstrated an unprecedented level of long-term stability of an LPA-driven FEL, starting with stable electron beam generation over more than 10 h and FEL operation of more than 8 h without operator intervention. This was achieved while maintaining a high level of shot-to-shot stability and FEL gain, comparable to the performance demonstrated earlier by Barber *et al.* in [17] over about 1 h of operation. Key to significantly exceed previously reported durations of continuous LPA-FEL operation [16,17,48] was the integration of multiple active stabilization techniques simultaneously, which drastically improved long-term stability of the LPA source and generated electron beams. The results represent a crucial step toward reliable operation of an FEL light source using electron bunches from an LPA. We discussed some of the techniques applied on the HTU system to stabilize the laser pulse, which have proved crucial in enabling this degree of reliability of the LPA. The setup and stabilization techniques presented here are fundamentally capable of delivering stable electron beams at energies up to 500 MeV, which will enable planned future efforts to reduce the undulator radiation wavelength toward  $\lambda = 30$  nm.

Investigation of the correlations between the undulator radiation and large number of LPA parameters recorded on every shot have proven to give valuable insights into the dynamics of the FEL process and will motivate and enable future efforts of LPA stabilization. Overall, these results serve as another powerful indication of the ability of the HTU system to act as a capable platform for long-term, LPA-driven FEL studies, and represent a big step toward the level of performance required for LPAs in general, to fulfill their promise as highly powerful, compact, and versatile next-generation particle accelerators.

Encouraged by the number of LPA parameters identified to show significant correlation to the FEL performance, we plan to develop sophisticated modeling techniques in the future, including digital twins, to conduct in-depth studies of the complex connections between LPA parameters, the experimental setup, undulator alignment, and the FEL performance.

## ACKNOWLEDGMENTS

This work was supported by the U.S. Department of Energy (DOE), Office of Science, the Office of Basic Energy Sciences, and the Office of High Energy Physics under Contract No. DE-AC02-05CH11231, through a CRADA with Tau Systems and by the Gordon and Betty Moore Foundation under Grant No. GBMF4898.

## DATA AVAILABILITY

The data that support the findings of this article are not publicly available upon publication because it is not technically feasible and/or the cost of preparing, depositing, and hosting the data would be prohibitive within the terms of this research project. The data are available from the authors upon reasonable request.

- 
- [1] T. Tajima and J. M. Dawson, Laser electron accelerator, *Phys. Rev. Lett.* **43**, 267 (1979).
  - [2] E. Esarey, C. B. Schroeder, and W. P. Leemans, Physics of laser-driven plasma-based electron accelerators, *Rev. Mod. Phys.* **81**, 1229 (2009).
  - [3] X. Wang *et al.*, Quasi-monoenergetic laser-plasma acceleration of electrons to 2 GeV, *Nat. Commun.* **4**, 1988 (2013).
  - [4] A. J. Gonsalves *et al.*, Petawatt laser guiding and electron beam acceleration to 8 GeV in a laser-heated capillary discharge waveguide, *Phys. Rev. Lett.* **122**, 084801 (2019).
  - [5] C. Aniculaesei *et al.*, The acceleration of a high-charge electron bunch to 10 GeV in a 10-cm nanoparticle-assisted wakefield accelerator, *Matter Radiat. Extremes* **9**, 014001 (2023).
  - [6] A. Picksley, J. Stackhouse, C. Benedetti, K. Nakamura, H. E. Tsai, R. Li, B. Miao, J. E. Shrock, E. Rockafellow, H. M. Milchberg, C. B. Schroeder, J. van Tilborg, E. Esarey, C. G. R. Geddes, and A. J. Gonsalves, Matched guiding and controlled injection in dark-current-free, 10-GeV-class, channel-guided laser-plasma accelerators, *Phys. Rev. Lett.* **133**, 255001 (2024).
  - [7] J. Faure, Y. Glinec, A. Pukhov, S. Kiselev, S. Gordienko, E. Lefebvre, J. P. Rousseau, F. Burgy, and V. Malka, A laser-plasma accelerator producing monoenergetic electron beams, *Nature (London)* **431**, 541 (2004).
  - [8] S. P. D. Mangles, C. D. Murphy, Z. Najmudin, A. G. R. Thomas, J. L. Collier, A. E. Dangor, E. J. Divall, P. S. Foster, J. G. Gallacher, C. J. Hooker, D. A. Jaroszynski, A. J. Langley, W. B. Mori, P. A. Norreys, F. S. Tsung, R. Viskup, B. R. Walton, and K. Krushelnick, Monoenergetic

- beams of relativistic electrons from intense laser–plasma interactions, *Nature (London)* **431**, 535 (2004).
- [9] B. Hidding, G. Pretzler, J. B. Rosenzweig, T. Königstein, D. Schiller, and D. L. Bruhwiler, Ultracold electron bunch generation via plasma photocathode emission and acceleration in a beam-driven plasma blowout, *Phys. Rev. Lett.* **108**, 035001 (2012).
- [10] L.-L. Yu, E. Esarey, C. B. Schroeder, J.-L. Vay, C. Benedetti, C. G. R. Geddes, M. Chen, and W. P. Leemans, Two-color laser-ionization injection, *Phys. Rev. Lett.* **112**, 125001 (2014).
- [11] X. Xu, F. Li, F. S. Tsung, K. Miller, V. Yakimenko, M. J. Hogan, C. Joshi, and W. B. Mori, Generation of ultrahigh-brightness pre-bunched beams from a plasma cathode for x-ray free-electron lasers, *Nat. Commun.* **13**, 3364 (2022).
- [12] C. G. R. Geddes, C. Toth, J. van Tilborg, E. Esarey, C. B. Schroeder, D. Bruhwiler, C. Nieter, J. Cary, and W. P. Leemans, High-quality electron beams from a laser wakefield accelerator using plasma-channel guiding, *Nature (London)* **431**, 538 (2004).
- [13] D. Jaroszynski, R. Bingham, E. Brunetti, B. Ersfeld, J. Gallacher, B. van der Geer, R. Issac, S. Jamison, D. Jones, M. de Loos, A. Lyachev, V. Pavlov, A. Reitsma, Y. Saveliev, G. Vieux, and S. Wiggins, Radiation sources based on laser–plasma interactions, *Phil. Trans. R. Soc. A* **364**, 689 (2006).
- [14] C. B. Schroeder, W. M. Fawley, E. Esarey, and W. P. Leemans, Design of an XUV FEL driven by the laser-plasma accelerator at the LBNL LOASIS facility, Technical Report No. LBNL–60154, Lawrence Berkeley National Laboratory, USA, 2006.
- [15] W. Wang, K. Feng, L. Ke, C. Yu, Y. Xu, R. Qi, Y. Chen, Z. Qin, Z. Zhang, M. Fang, J. Liu, K. Jiang, H. Wang, C. Wang, X. Yang, F. Wu, Y. Leng, J. Liu, R. Li, and Z. Xu, Free-electron lasing at 27 nanometres based on a laser wakefield accelerator, *Nature (London)* **595**, 516 (2021).
- [16] M. Labat *et al.*, Seeded free-electron laser driven by a compact laser plasma accelerator, *Nat. Photonics* **17**, 150 (2023).
- [17] S. K. Barber, F. Kohrell, C. Doss, K. Jensen, C. Berger, F. Isono, Z. Eisentraut, S. Schröder, A. J. Gonsalves, K. Nakamura, G. R. Plateau, R. A. van Mourik, M. Gracia-Linares, L. Labun, B. M. Hegelich, S. V. Milton, C. G. R. Geddes, J. Osterhoff, C. B. Schroeder, E. Esarey, and J. van Tilborg, Greater than 1000-fold gain in a free-electron laser driven by a laser-plasma accelerator with high reliability, *Phys. Rev. Lett.* **135**, 055001 (2025).
- [18] M. Galletti, R. Assmann, M. E. Couprie, M. Ferrario, L. Giannessi, A. Irman, R. Pompili, and W. Wang, Prospects for free-electron lasers powered by plasma-wakefield-accelerated beams, *Nat. Photonics* **18**, 780 (2024).
- [19] F. Grüner, S. Becker, U. Schramm, T. Eichner, M. Fuchs, R. Weingartner, D. Habs, J. Meyer-ter Vehn, M. Geissler, M. Ferrario, L. Serafini, B. van der Geer, H. Backe, W. Lauth, and S. Reiche, Design considerations for table-top, laser-based VUV and X-ray free electron lasers, *Appl. Phys. B* **86**, 431 (2007).
- [20] C. Berger, S. Barber, F. Isono, K. Jensen, J. Natal, A. Gonsalves, and J. van Tilborg, Active nonperturbative stabilization of the laser-plasma-accelerated electron beam source, *Phys. Rev. Accel. Beams* **26**, 032801 (2023).
- [21] K. Jensen, S. Barber, C. Berger, C. Doss, F. Kohrell, S. Coleman, N. Cook, J. Edelen, J. Einstein-Curtis, and J. van Tilborg, Improved laser-plasma accelerator stability via high-bandwidth longitudinal focal position stabilization of 100 TW-class laser system, *Phys. Rev. Accel. Beams* **28**, 092802 (2025).
- [22] A. R. Maier, N. M. Delbos, T. Eichner, L. Hübner, S. J alas, L. Jeppe, S. W. Jolly, M. Kirchen, V. Leroux, P. Messner, M. Schnepp, M. Trunk, P. A. Walker, C. Werle, and P. Winkler, Decoding sources of energy variability in a laser-plasma accelerator, *Phys. Rev. X* **10**, 031039 (2020).
- [23] F. Kohrell, S. Barber, K. Jensen, C. Doss, C. Berger, C. Schroeder, E. Esarey, F. Grüner, and J. van Tilborg, Investigation of correlations between spectral phase fluctuations of the laser pulse and the performance of an LPA, *Nucl. Instrum. Methods Phys. Res., Sect. A* **1073**, 170267 (2025).
- [24] G. White and T. Raubenheimer, Transverse jitter tolerance issues for beam-driven plasma accelerators, in *Proceedings of the 10th International Particle Accelerator Conference IPAC-2019 (JACoW, Geneva, Switzerland, 2019)*, p. 4.
- [25] L. Ke, K. Feng, W. Wang, Z. Qin, C. Yu, Y. Wu, Y. Chen, R. Qi, Z. Zhang, Y. Xu, X. Yang, Y. Leng, J. Liu, R. Li, and Z. Xu, Near-GeV electron beams at a few per-mille level from a laser wakefield accelerator via density-tailored plasma, *Phys. Rev. Lett.* **126**, 214801 (2021).
- [26] 2023 P5 report: Exploring the Quantum Universe, <https://www.usparticlephysics.org/2023-p5-report/index.html>.
- [27] J. N. Butler *et al.*, Report of the 2021 U.S. community study on the future of particle physics (Snowmass 2021) summary chapter, [arXiv:2301.06581](https://arxiv.org/abs/2301.06581).
- [28] D. Strickland and G. Mourou, Compression of amplified chirped optical pulses, *Opt. Commun.* **55**, 447 (1985).
- [29] S. Bulanov, N. Naumova, F. Pegoraro, and J. Sakai, Particle injection into the wave acceleration phase due to nonlinear wake wave breaking, *Phys. Rev. E* **58**, R5257 (1998).
- [30] H. Suk, N. Barov, J. B. Rosenzweig, and E. Esarey, Plasma electron trapping and acceleration in a plasma wake field using a density transition, *Phys. Rev. Lett.* **86**, 1011 (2001).
- [31] C. G. R. Geddes, K. Nakamura, G. R. Plateau, C. Toth, E. Cormier-Michel, E. Esarey, C. B. Schroeder, J. R. Cary, and W. P. Leemans, Plasma-density-gradient injection of low absolute-momentum-spread electron bunches, *Phys. Rev. Lett.* **100**, 215004 (2008).
- [32] M. Migliorati, A. Bacci, C. Benedetti, E. Chiadroni, M. Ferrario, A. Mostacci, L. Palumbo, A. R. Rossi, L. Serafini, and P. Antici, Intrinsic normalized emittance growth in laser-driven electron accelerators, *Phys. Rev. ST Accel. Beams* **16**, 011302 (2013).
- [33] N. Majernik, S. K. Barber, J. van Tilborg, J. B. Rosenzweig, and W. P. Leemans, Optimization of low aspect ratio, iron dominated dipole magnets, *Phys. Rev. Accel. Beams* **22**, 032401 (2019).
- [34] A. R. Maier, A. Meseck, S. Reiche, C. B. Schroeder, T. Seggebrock, and F. Grüner, Demonstration scheme for a

- laser-plasma-driven free-electron laser, *Phys. Rev. X* **2**, 031019 (2012).
- [35] R. Carr, M. Cornacchia, P. Emma, H.-D. Nuhn, B. Poling, R. Ruland, E. Johnson, G. Rakowsky, J. Skaritka, S. Lidia, P. Duffy, M. Libkind, P. Frigola, A. Murokh, C. Pellegrini, J. Rosenzweig, and A. Tremaine, Visible-infrared self-amplified spontaneous emission amplifier free electron laser undulator, *Phys. Rev. ST Accel. Beams* **4**, 122402 (2001).
- [36] A. Tremaine, X. J. Wang, M. Babzien, I. Ben-Zvi, M. Cornacchia, H.-D. Nuhn, R. Malone, A. Murokh, C. Pellegrini, S. Reiche, J. Rosenzweig, and V. Yakimenko, Experimental characterization of nonlinear harmonic radiation from a visible self-amplified spontaneous emission free-electron laser at saturation, *Phys. Rev. Lett.* **88**, 204801 (2002).
- [37] A. Murokh *et al.*, Properties of the ultrashort gain length, self-amplified spontaneous emission free-electron laser in the linear regime and saturation, *Phys. Rev. E* **67**, 066501 (2003).
- [38] H.-D. Nuhn, FEL trajectory analysis for the VISA experiment, Technical Reports No. SLAC-PUB-7913, No. SLAC-PUB-9912, Stanford Linear Accelerator Center, Stanford University, 1998, <https://www.slac.stanford.edu/pubs/slacpubs/7750/slac-pub-7913.pdf>.
- [39] P. Frigola *et al.*, Initial gain measurements of an 800 nm SASE FEL, VISA, *Nucl. Instrum. Methods Phys. Res., Sect. A* **475**, 339 (2001); V. N. Litvinenko and Y. K. Wu, FEL2000: Proceedings of the 22nd international free electron laser conference and 7th FEL users workshop, *Nucl. Instrum. Methods Phys. Res., Sect. A* **475**, v (2001).
- [40] R. Trebino and E. Zeek, The autocorrelation, the spectrum, and phase retrieval, in *Frequency-Resolved Optical Gating: The Measurement of Ultrashort Laser Pulses* (Springer US, Boston, MA, 2000), pp. 61–99.
- [41] R. Trebino, *Frequency-Resolved Optical Gating: The Measurement of Ultrashort Laser Pulses* (Springer US, Boston, MA, 2000).
- [42] G. R. Plateau, N. H. Matlis, C. G. R. Geddes, A. J. Gonsalves, S. Shiraishi, C. Lin, R. A. Van Mourik, and W. P. Leemans, Wavefront-sensor-based electron density measurements for laser-plasma accelerators, *Rev. Sci. Instrum.* **81**, 033108 (2010).
- [43] F. Isono, J. v. Tilborg, S. K. Barber, J. Natal, C. Berger, H.-E. Tsai, T. Ostermayr, A. Gonsalves, C. Geddes, and E. Esarey, High-power non-perturbative laser delivery diagnostics at the final focus of 100-TW-class laser pulses, *High Power Laser Sci. Eng.* **9**, e25 (2021).
- [44] M. Kirchen, S. Jalas, P. Messner, P. Winkler, T. Eichner, L. Hübner, T. Hülsenbusch, L. Jeppe, T. Parikh, M. Schnepf, and A. R. Maier, Optimal beam loading in a laser-plasma accelerator, *Phys. Rev. Lett.* **126**, 174801 (2021).
- [45] S. Jalas, M. Kirchen, C. Braun, T. Eichner, J. Gonzalez, L. Hübner, T. Hülsenbusch, P. Messner, G. Palmer, M. Schnepf, C. Werle, P. Winkler, W. Leemans, and A. Maier, Tuning curves for a laser-plasma accelerator, *Phys. Rev. Accel. Beams* **26**, 071302 (2023).
- [46] R. Trebino, K. W. DeLong, D. N. Fittinghoff, J. N. Sweetser, M. A. Krumbügel, B. A. Richman, and D. J. Kane, Measuring ultrashort laser pulses in the time-frequency domain using frequency-resolved optical gating, *Rev. Sci. Instrum.* **68**, 3277 (1997).
- [47] S. Akturk, M. Kimmel, P. O’Shea, and R. Trebino, Measuring spatial chirp in ultrashort pulses using single-shot frequency-resolved optical gating, *Opt. Express* **11**, 68 (2003).
- [48] W. Wang, K. Feng, L. Ke, C. Yu, Y. Xu, R. Qi, Y. Chen, Z. Qin, Z. Zhang, M. Fang, J. Liu, K. Jiang, H. Wang, C. Wang, X. Yang, F. Wu, Y. Leng, J. Liu, R. Li, and Z. Xu, Free-electron lasing at 27 nanometres based on a laser wakefield accelerator, *Nature (London)* **595**, 516 (2021).